Rayleigh wave phase velocity analysis of the Ross Sea, Transantarctic Mountains, and East Antarctica from a temporary seismograph array

Jesse F. Lawrence,[1,2] Douglas A. Wiens,[1] Andrew A. Nyblade,[3] Sridhar Anandakrishnan,[3] Patrick J. Shore,[1] and Donald Voigt[3]

Received 2 May 2005; revised 4 October 2005; accepted 12 January 2006; published 13 June 2006.

[1] This study analyzes Rayleigh wave phase velocities from the Ross Sea (RS) region of the West Antarctica rift system, the Transantarctic Mountains (TAMs), and part of East Antarctica (EA). The Transantarctic Mountain Seismic Experiment deployed 41 three-component broadband seismometers, which provide new data for high-resolution two-dimensional maps demonstrating crustal and uppermost mantle seismic velocity anomalies. The short-period (16–25 s) phase velocity maps are consistent with changes in crustal thickness from ~20 km under the RS to ~35 km beneath the TAMs and EA. Long-period (75–175 s) phase velocity maps indicate high mantle velocities beneath EA, low velocity beneath the RS, and a transition between the two between 50 and 150 km inland. The EA phase velocities in the region adjacent to the TAM exhibit a directional pattern consistent with 2 ± 1% azimuthal anisotropy with a NE-SW fast direction. The structure of the RS is similar to continental rifting environments elsewhere, with a pronounced low-velocity zone in the ~80–220 km depth range, whereas EA shows a typical continental cratonic structure with high velocities between the 80 and 220 km depth range.

Citation: Lawrence, J. F., D. A. Wiens, A. A. Nyblade, S. Anandakrishnan, P. J. Shore, and D. Voigt (2006), Rayleigh wave phase velocity analysis of the Ross Sea, Transantarctic Mountains, and East Antarctica from a temporary seismograph array, *J. Geophys. Res.*, *111*, B06302, doi:10.1029/2005JB003812.

1. Introduction

[2] This study analyzes Rayleigh wave phase velocities in order to seismically image the crustal and upper mantle structure beneath part of the Ross Sea, the Transantarctic Mountains, and East Antarctica (Figure 1). The study region crosses a major lithospheric boundary between East Antarctica, which is predominantly a Precambrian craton [e.g., *Tingley*, 1991], and West Antarctica, which is much younger, with Cenozoic tectonic activity [e.g., *Behrendt et al.*, 1991b]. Data from this study come from the Transantarctic Mountain Seismic Experiment (TAMSEIS), the first large-scale broadband seismic experiment in Antarctica. TAMSEIS deployed 41 seismometers between the Ross Sea and the Vostok Subglacial Highlands from November 2000 to December 2003.

[3] Geophysically, the study area can be broken into three main tectonic regions: the Ross Sea region (RS) of the West Antarctic rift system (WARS), the Transantarctic Mountains (TAMs), and the East Antarctica craton (EA). The WARS has sea level or lower bedrock elevations and 20–35 km thick crust that was thinned in many places by extension during the Cretaceous and Cenozoic [*Behrendt et al.*, 1991a; *Fitzgerald et al.*, 1986]. This study images the WARS in the western part of the Ross Sea, an area of submerged, extended continental crust [*Davey*, 1981]. The Terror Rift, a major extensional graben [*Cooper et al.*, 1987], and several large volcanoes, including Mount Erebus, lie within the western Ross Sea and have been variously ascribed to continental extension or mantle plume origin [*Kyle et al.*, 1992; *Storey*, 1996]. Crustal thickness in the Terror Rift region has been estimated at 18–25 km [*Behrendt*, 1999; *Brancolini et al.*, 1995; *Busetti et al.*, 1999; *Cooper et al.*, 1997].

[4] The Transantarctic Mountains are approximately 4000 km long and 300 km wide, dividing EA from the WARS with peaks that rise over 4 km above sea level. Crustal thickness estimates under the TAMs vary between 20 and 45 km [*ten Brink et al.*, 1993, 1997; *Bannister et al.*, 2003; *Kanao et al.*, 2002]. The TAMs differ from most mountain ranges of similar size and lateral extent in that they lack evidence of compressional structures.

[5] East Antarctica is marked by high elevations [*Cogley*, 1984], but bedrock exposure is limited to coastal areas and thus little is known about the interior of the craton. On the basis of geologic studies around the periphery, East Ant-

[1]Department of Earth and Planetary Sciences, Washington University, St. Louis, Missouri, USA.
[2]Now at Scripps Institute of Oceanography, University of California, San Diego, La Jolla, California, USA.
[3]Department of Geosciences, Pennsylvania State University, State College, Pennsylvania, USA.

0148-0227/06/2005JB003812$09.00

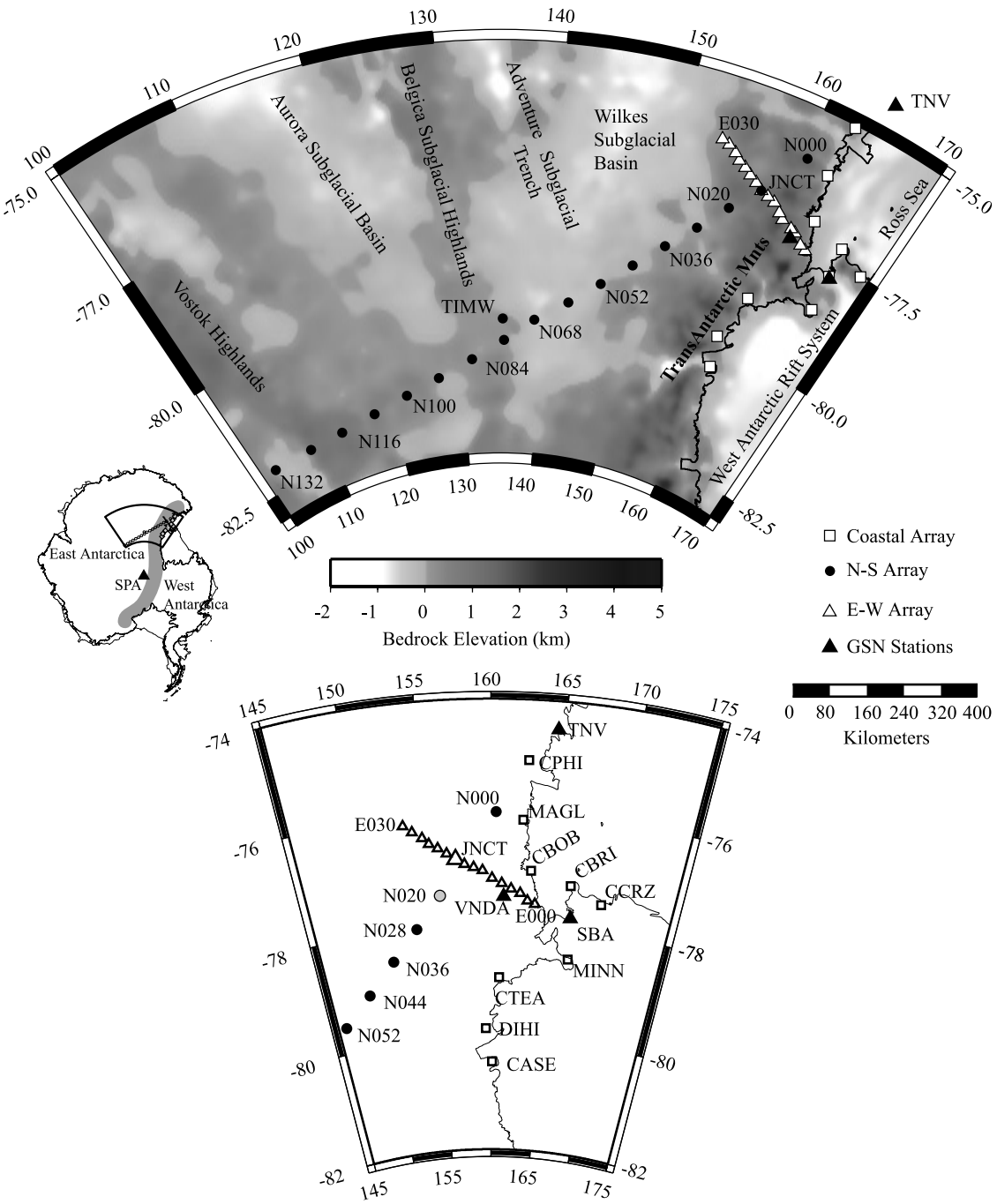

Figure 1. (top) Map of the seismic stations used in this study overlaid on bedrock topography from BEDMAP [*Lythe et al.*, 2001]. The triangles, circles, and squares show seismometer locations. (bottom) Inset map of stations in the Ross Island and coastal regions.

arctica is likely a Precambrian craton that amalgamated with other cratons to form the Paleozoic supercontinent, Gondwana [*Tingley*, 1991; *Dalziel*, 1992]. Surface wave tomographic studies show fast upper mantle velocities beneath East Antarctica, consistent with cratonic regions elsewhere in the world [*Roult and Rouland*, 1994; *Danesi and Morelli*, 2001; *Ritzwoller et al.*, 2001]. Crustal thickness is essentially unknown in the interior of East Antarctica, and estimates range from 30 km [*Studinger et al.*, 2003] to 65 km [*Groushinsky and Sazhina*, 1982], with most around 35–45 km [*Bentley*, 1991].

[6] Large-scale surface wave velocity studies [*Roult and Rouland*, 1994; *Danesi and Morelli*, 2001; *Ritzwoller et al.*, 2001] demonstrate that the TAMs lie near the boundary between fast East Antarctica and slow West Antarctica upper mantle. These studies present smoothed models showing sharp lateral velocity gradients signifying a major lithospheric boundary between East and West Antarctica. However, because of the relative lack of seismicity and seismometers in the Antarctic interior the resolution of these seismic models is limited to 500–1000 kilometers. Consequently the location of the boundary and the role of mantle

Table 1. Seismic Stations

Station	Latitude	Longitude
	TAMSEIS Coastal Array	
CPHI	−75.0745	162.6484
MAGL	−76.1381	162.4083
CBOB	−77.0342	163.1707
CBRI	−77.2516	166.4266
CCRI	−77.5166	169.0947
MINN	−78.5504	166.8800
CTEA	−78.9439	160.7643
DIHI	−79.8491	159.4800
CASE	−80.4481	160.1262
	TAMSEIS East-West Array	
E000	−77.6262	163.6175
E002	−77.575	163.0078
E004	−77.4133	162.0661
E006	−77.3703	161.6256
E008	−77.2817	160.5033
E010	−77.1853	160.0098
E012	−77.0461	159.3247
E014	−76.9898	158.6217
E018	−76.8234	157.2237
E020	−76.7295	156.5472
E022	−76.628	155.9025
E024	−76.5346	155.2500
E026	−76.4248	154.7582
E028	−76.3075	154.0384
E030	−76.251	153.3793
	TAMSEIS North-South Array	
N000	−76.0087	160.3784
JNCT	−76.9288	157.9012
N020	−77.4678	155.8175
N028	−78.0296	153.6509
N036	−78.5508	151.2776
N044	−79.0692	148.6159
N052	−79.5441	145.7489
N060	−80.0000	142.5936
N068	−80.3911	138.9200
N076	−80.8061	135.4326
N084	−81.1601	131.4673
N092	−81.4621	126.9822
N100	−81.691	122.4672
N108	−81.8791	117.6036
N116	−82.0094	112.5698
N124	−82.0741	107.6413
N132	−82.0751	101.9539
	GSN Stations	
TNV	−74.7000	164.1200
VNDA	−77.5139	161.8456
SBA	−77.8491	166.7573
SPA	−90.0000	0.0000
QSPA	−89.9279	145.0000

structure in the mountain building processes of the TAM are ill resolved. *Bannister et al.* [2000] used several Global Seismic Network stations (VNDA, TNV, and SBA) to demonstrate that the mantle shear wave velocities changed from a maximum of 6% slow beneath the WARS to 2% slow beneath the TAMs within just 100 km lateral distance.

[7] In this paper we describe the data and methods used to analyze Rayleigh wave phase velocities. We employ an array analysis method modified from the work of *Menke and Levin* [2002] to solve for the variation from the great circle path assumed by many studies, which enables more precise estimation of the interstation phase velocity. We then calculate average regional structures for WARS, EA, and TAMs to demonstrate the general variations between the regions. We examine azimuthal anisotropy for the intersection of the two main TAMSEIS lines where sufficient azimuthal coverage is possible with minimal lateral structural contamination. We then perform a tomographic inversion for phase velocity maps using singular value decomposition. Resolution tests are computed to determine the most appropriate parameterization. Finally, the resulting phase velocity maps are discussed and interpreted.

2. Data and Measurements

2.1. TAMSEIS Deployment

[8] This study employs vertical component, broadband seismic data recorded at 46 seismic stations (41 Transantarctic Mountain Seismic Experiment stations and 5 Global Seismic Network stations; VNDA, SBA, TNV, SPA, QSPA) in Antarctica during the austral summers between November 2000 and December 2003. The broadband stations were powered by battery and solar power during the Austral summers (October–March), and used heating elements to protect and stabilize the seismic equipment from the extreme cold. TAMSEIS consists of three broadband subarrays (Figure 1 and Table 1). The first is a 16-station linear array striking roughly east-west across the TAMs, with approximately 20 km interstation spacing, spanning 300 km. The second subarray consists of 17 stations (JNCT is shared with subarray 1) striking NNE-SSW from Terra Nova (TNV), with 80 km interstation spacing, reaching 1400 km into the Antarctic interior. The third, 9-station subarray is dispersed roughly north-south along the coast and on Ross Island. Eight of the TAMSEIS stations were deployed in December 2000, and the other 33 were deployed in late 2001.

[9] Events with Ms greater than 5.8 and with distances between 30 and 150 degrees were considered for analysis. Each waveform was visually inspected to ensure high-quality data. The original data, sampled at 20 or 40 samples per second, were resampled at 2 samples per second. Trends were removed from the data and the instrument response was removed to eliminate variations between the different types of broadband sensors used in the experiment.

2.2. Phase Velocity Measurements

[10] Interstation phase velocities (V_{ij}) are determined by applying the multiple filter technique (MFT) [*Dziewonski et al.*, 1969] cross correlelogram of the vertical Rayleigh wave phase matched filters [*Herrin and Goforth*, 1977] for any two stations, i and j. First, a cross correlelogram is calculated for each pair of vertical seismograms recorded at each set of broadband stations within the network for a single earthquake. The MFT simply applies a series of narrow band-pass filters to each cross correlelogram with varying set of center frequencies. The peak of each cross correlelogram provides a time shift associated with each period, which can be converted into a phase velocity using an assumed interstation distance. Applying the multiple filter technique after cross correlation reduces computation time and improves the measurement by decreasing the summation of errors. The reduction in computation time is important because, as discussed below, interstation phase velocities are calculated for all ($N[N-1]/2$) station pairs within the network. Phase velocity uncertainties become

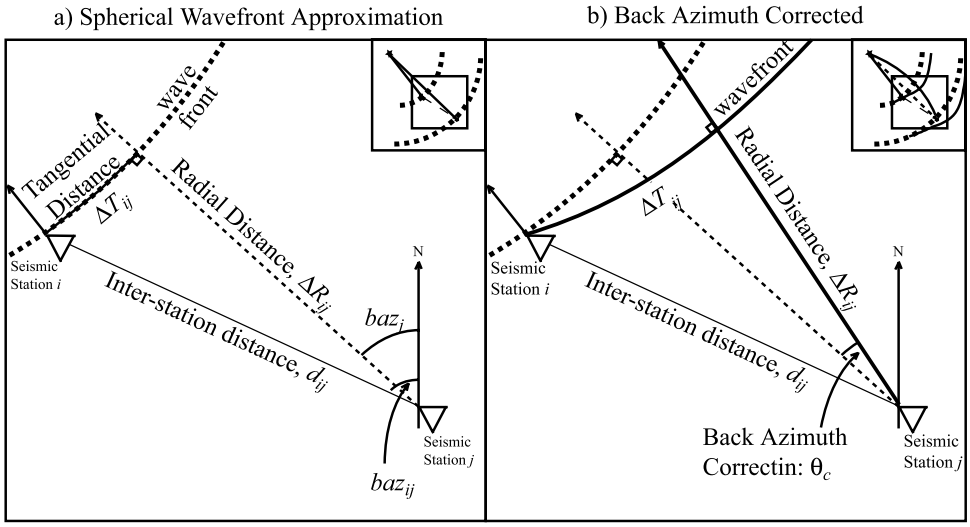

Figure 2. (a) Geometry for a spherical wavefront approximation appropriate for a laterally homogeneous earth. The wave propagation distance is measured along the great circle path connecting source and receiver. (b) Geometry including a back azimuth correction for wavefront distortion outside the array. The propagation distance is measured along a normal (perpendicular) direction to the wavefront.

large for velocity measurements associated with short interstation distances. At short distances small errors in phase time delays may represent significant errors in phase velocity. The uncertainty in phase time delay measurements is approximately proportional to the wavelength. Therefore we require that the interstation ray path distance be at least 1/4 the wavelength. This requirement reduces the number of measurements and also the spatial resolution for longer periods because short-distance phase velocities are not used.

[11] Lateral heterogeneity between the source and the array may distort the wavefront such that the apparent back azimuth at the array deviates from the great circle back azimuth (Figure 2). *Menke and Levin* [2002] introduced a method for determining the effective wavefront back azimuth from three or more interstation travel times. By inverting the vector, $\mathbf{\Delta t}$, containing the $N[N-1]/2$ interstation travel times, Δt_{ij}, and the matrix, $\mathbf{\Delta x}$, containing interstation distances in orthogonal directions, x_{Rij} and x_{Tij}, we can calculate orthogonal measures of slowness:

$$\mathbf{p} = \left[\mathbf{\Delta x^T \Delta x}\right]^{-1} \mathbf{\Delta x^T \Delta t}, \tag{1}$$

where $\mathbf{p}$ is the slowness vector in orthogonal directions, p_R and p_T. We use a spherical geometry rather than the Cartesian geometry of *Menke and Levin* [2002] by rotating the orthogonal distances into the spherical wavefront reference frame. In the wavefront reference frame the orthogonal distances ($\mathbf{\Delta x}$) are the radial distance (ΔR_{ij}), along the ray path from event-to-station, and tangential distance (ΔT_{ij}), along wavefront. The rotation takes the form,

$$\begin{bmatrix} \Delta R_{ij} \\ \Delta T_{ij} \end{bmatrix} = \begin{bmatrix} \cos\left(baz_j - baz_{ij}\right) \\ \sin\left(baz_j - baz_{ij}\right) \end{bmatrix} d_{ij}, \tag{2}$$

where baz_j and baz_{ij} are the event-to-station and station-to-station back azimuths as measured from the more distant station, j, and d_{ij} is the greater-circle interstation distance between stations i and j. The back azimuth correction is provided by $\theta = \tan^{-1}(p_T/p_R)$.

[12] We use an iterative process to determine the back azimuth correction for either the whole network or part of the network with the assumption that the back azimuth correction varies only slightly within the array. The phase velocities are first estimated assuming the great circle path for 30 different central periods. The 30 central periods are 16, 18, 20, 22, 23, 26, 29, 32, 36, 40, 44, 48, 52, 56, 60, 65, 70, 75, 80, 85, 90, 100, 110, 120, 130, 140, 150, 160, 170, and 180. The width of each Gaussian band-pass filter decreases as $1/T_c$ where T_c is the central period. The velocities are plotted as a function of period. The phase velocities are quality controlled at this point to reduce error in the back azimuth calculation, eliminating outliers. While subjectively selected, outliers are loosely defined here as any set of periods having greatly different phase velocities ($\delta \ln c > 10\%$) from contiguous periods. The back azimuth corrections are calculated for each event and frequency, and the interstation phase velocities are adjusted accordingly. These adjusted velocities are plotted as a function of the difference between station-to-station back azimuth and corrected event-to-station back azimuth, $\varphi = (\theta_c + baz_j) - baz_{ij}$. The correct back azimuth minimizes velocity variations as a function of φ. At this point outliers are removed when they deviate significantly from the mean inverted slowness, $\mathbf{p}$. This ensures a more stable back azimuth solution. Once the correct back azimuth is calculated for each period, the phase velocity curves are replotted as a function of period. Finally, the phase velocity curves are repicked with the correct back azimuth correction for each period. While all interstation phase velocities are considered for the back azimuth calculation, only interstation phase

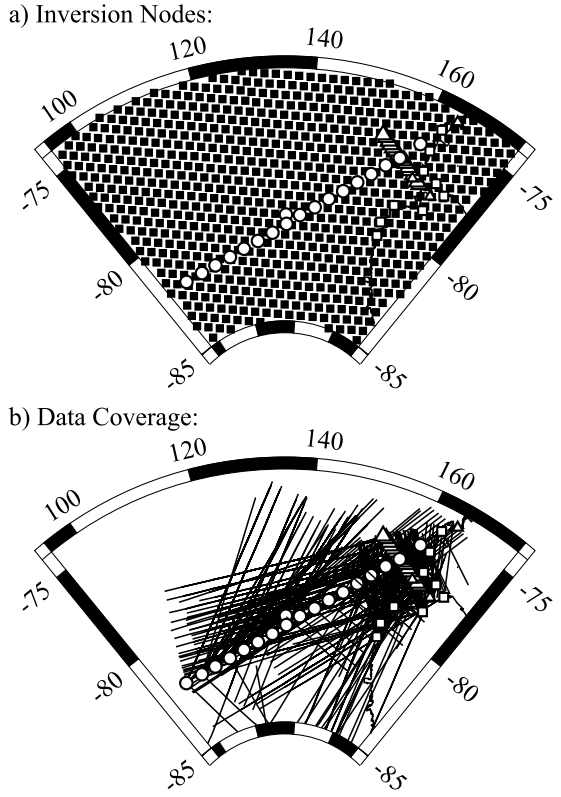

Figure 3. (a) Nodes used for phase velocity inversion (squares). (b) Surface wave ray paths used in the tomographic inversion. Note that most paths completely overlap with other paths, so they are not visible.

velocities having low off-axis angles, $|\varphi| < 20$ degrees, are retained for further analysis.

[13] We test for variation of the incident wavefront back azimuth within the network by calculating the back azimuth with three geographically defined subnetworks of stations. The first station geometry consists of all stations within 140 km from the coast. The second data subset consists of all stations more than 100 km west of the coast and north of station N044. The third data subset uses only paths from array stations to stations south of N044. This third data subset is limited to earthquakes to the northeast of TAMSEIS, but is the only reasonable back azimuth test for the stations south of N044. For the five (3 for subset 3) earthquakes with the highest signal-to-noise ratio recorded at more than 5 stations in each subarray the back azimuth correction differs by less than 1° from the back azimuth calculated for the whole array. Consequently, we feel confident that the array analysis using the whole network is sufficient, rather than requiring subsections of the data.

[14] The back azimuth corrections themselves vary by as much as 9° from the event-to-station greater circle path. Earthquakes roughly north or south of TAMSEIS require the highest back azimuth variation. These roughly north-south back azimuths typically shift by as much as 4° to the east at short periods (16–25 s), and as much as 7° to the west at long periods (100–180 s), which suggests a distorted wavefront resulting from structural variations outside the array. Earthquakes to the east and west of TAMSEIS required smaller (<2°) back azimuth corrections for both long and short periods. Phase velocities are considered unreliable and discarded when back azimuth corrections change rapidly or sporadically with period ($\Delta\theta_c > 2$ degree between periods). Discontinuous changes in back azimuth correction cause discontinuous changes in the measured phase velocity, which is unreasonable. The greatest change in back azimuth correction as a function of period occurs at shorter periods (16–25 s).

[15] The observation of systematic changes in back azimuth correction indicates that long-wavelength wavefront perturbations due to lateral heterogeneity outside the TAMSEIS network are being accounted for. Consequently, the back azimuth corrections reduce the sensitivity to large-scale seismic anomalies outside the TAMSEIS network. The similarity between back azimuth corrections for subsections of the network suggests that small-scale anomalies outside the array are less important. While small-scale anomalies outside the network could effect individual measurements, the consistency of results from measurements regardless of back azimuth and back azimuth correction, suggests that small-scale anomalies outside the network have little effect. Nevertheless, care is taken in later analyses to minimize potential effects of such anomalies by averaging results or smoothing the inversions.

[16] When applied to the available data, this method produces 1684 interstation phase velocity curves for all stations and all earthquakes (Figure 3). Each curve is constructed from interstation phase velocities measured at up to 30 periods from 16 to 180 s depending on the number of outliers in each curve. The number of measurements for all stations and all earthquakes at each period varies from 1021 to 1603, with an average of 1122. The total number of interstation phase velocity measurements including all stations and all periods for all earthquakes is 33,657. The best coverage occurs between 33 and 110 s. At longer periods the number of measurements drops off because of limited frequency sensitivity for some seismometers and the restriction that the interstation paths must be longer than 1/4 the wavelength. Increased noise, short-wavelength wavefront perturbations and the rapid change in velocity with period are greater at high frequencies, making phase velocity measurement more difficult for short periods.

3. Analysis and Results

3.1. Average Dispersion Curves

[17] The average phase velocity curve for the TAMSEIS experiment is well constrained and has a significant standard deviation (Figure 4). We calculate the average phase velocity using a weighted average of the inverted slowness values determined with the array analysis for each event. The weight for each individual event phase velocity curve is proportional to the number of interstation paths used in each slowness inversion. The standard deviation is determined from the L2 misfit between the individual interstation measurements and the average curve. The phase velocities are typical for continental regions. The large standard deviation is due to lateral heterogeneity. Figure 5a demonstrates the similarity between the phase velocity curves associated with similar ray paths from two different earthquakes. Figure 5b demonstrates the significant difference

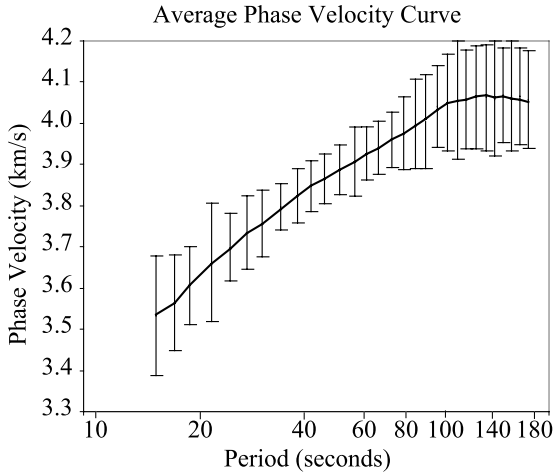

Figure 4. Average phase velocity curve for the whole region formed from a weighted average of individual event dispersion curves. The error bars represent 1 standard deviation from the mean phase velocity curve. The large standard deviation results mostly from significant lateral heterogeneity within the study region.

between phase velocities measured in East Antarctica and the Transantarctic Mountains from the same event. This result is consistent with the observations of *Bannister et al.* [2000].

[18] Regional weight-averaged phase velocities are calculated by applying the array method to three subsets of data corresponding to the three tectonic regions; EA, TAM, and RS. The EA subset includes only stations west of 100 km inland from the coast. The TAMs subset includes only stations between the coast and 140 km inland from the coast. The RS subset includes only stations less than 20 km from the coast and on Ross Island. The weight averaged phase velocities of the EA and RS tectonic regions are significantly different (Figure 6). The standard deviations from these regional averages are much less than the standard deviations from the overall average shown in Figure 4. The deviation from the mean TAMs phase velocity curve is higher than for EA or RS. Beneath the TAMs, phase velocity curves transition between EA and WARS end-members.

3.2. Average One-Dimensional Velocity Structures

[19] We invert phase velocities for three representative one-dimensional (1-D) shear velocity models that best fit

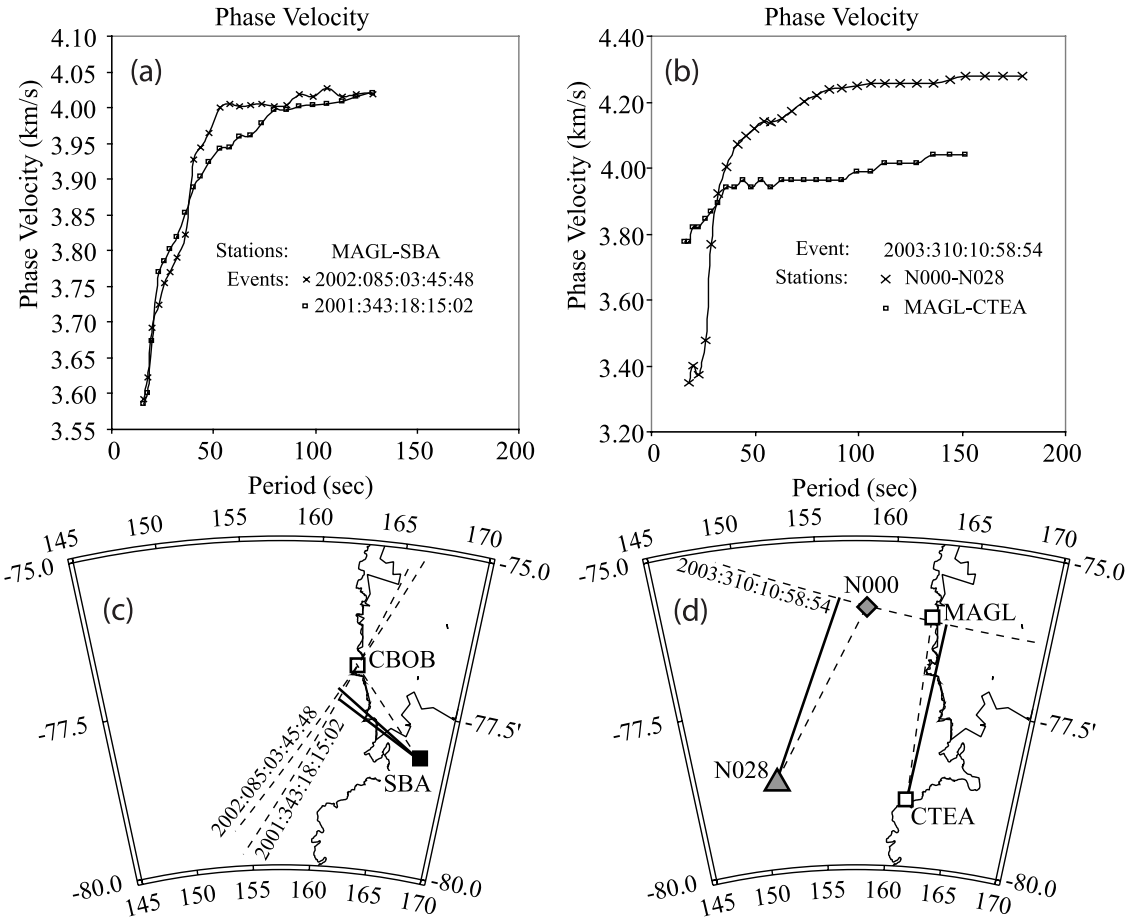

Figure 5. (a) Similarity between phase velocities from similar ray paths but different earthquakes. (b) Large difference between the phase velocities from dissimilar paths from the same earthquake. (c and d) Station locations and ray path geometries for Figures 5a and 5b, respectively. The dashed curves are the great circle paths between stations. The solid curves represent the wave propagation paths as calculated by the back azimuth correction.

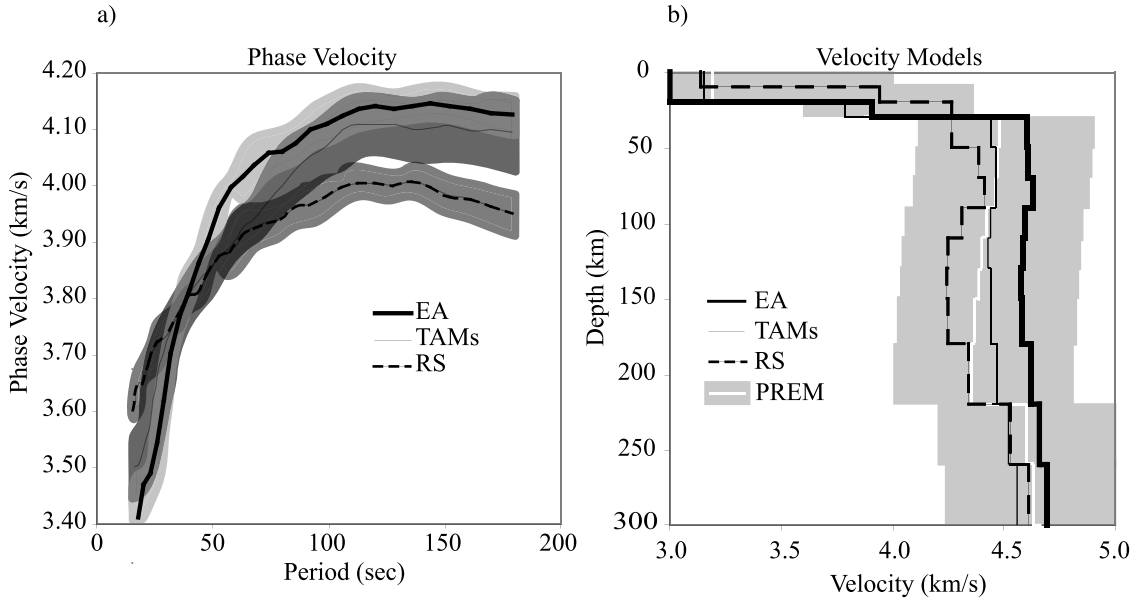

Figure 6. (a) Average phase velocity curves for the Ross Sea region (RS), the Transantarctic Mountains (TAMs), and East Antarctica (EA). The shaded areas represent the standard deviation from the average phase velocity curves for EA (light gray), RS (medium gray), and TAMs (dark gray). (b) NGA solutions for 12-layer smoothed shear velocity models. The shaded area is the provided model space.

average phase velocity curves for each of the three regions (East Antarctica, Ross Sea, and the Transantarctic Mountains, Figure 6). We employed the niching genetic algorithm (NGA) [*Koper et al.*, 1999; *Lawrence and Wiens*, 2004; *Mahfoud*, 1995] to invert the phase velocities. For details on the NGA algorithm and its application to seismic data, see *Koper et al.* [1999] and *Lawrence and Wiens* [2004].

[20] The misfit cost minimized by the NGA inversion is described in equation (3),

$$Cost = \left[\sqrt{\sum_{i=3}^{N_{lyr}-1}\left(\delta V_{S_{i+1}} - \delta V_{S_i}\right)^2}\right]^{RW} \cdot \left[\sqrt{\sum_{k=1}^{M}\left(D_{obs_k} - D_{syn_k}\right)^2 \Big/ M}\right], \quad (3)$$

where δV_S is the shear velocity perturbation from an augmented PREM [*Dziewonski and Anderson*, 1981], RW is the roughness weighting, M is the number of observed, D_{obs}, and synthetic, D_{syn}, Rayleigh phase velocity pairs. The smoothing is not applied for the uppermost two layers because we assume significant velocity perturbations exist on either side of the Moho. For each phase velocity curve the NGA runs for 250 generations, with 4 demes and 20 models in each deme, adding up to a search of 20,000 models. The roughness weighting is set at 0.5 but results in similar smoothness for RW values between 0.25 and 1.

[21] The layers are parameterized such that they are similar to PREM, but with several significant modifications. First, the crustal thickness is changed to match the preliminary results of receiver function analysis performed by *Lawrence et al.* [2006] and the previous results of *Bannister et al.* [2003] and *Kanao et al.* [2002]. We use a two-layer 20 km thick crust for the RS and a two-layer 35 km thick crust for EA and the TAMs. Second, a 2 km thick ice layer is added to the East Antarctic model in order to account for the thick ice layer observed there. The ice shear velocity is assumed to be V_S = 1.5 km s^{-1}. Third, all layers are assumed to be constant velocity rather than gradients. We use 12 layers that are allowed to vary between −10% and +10% from PREM.

[22] The results show that East Antarctic seismic velocities are continuously more than 0.25 km s^{-1} faster than those of West Antarctica between 80 and 220 km depth (Figure 6b), but are consistently faster for all depths below 30 km. The Transantarctic Mountains 1-D velocity model lies between the models of East and West Antarctica, favoring West Antarctica between 50 and 80 km and East Antarctica between 80 and 220 km (Figure 6b). The large scatter from the average phase velocity curves shown in Figure 6a and the overlap between these scatters indicate both large- and small-scale variations, which are analyzed below through phase velocity inversion. The scatter is largest in the TAMs region where the velocities likely vary from RS structure to EA structure.

3.3. Phase Velocity Anisotropy

[23] We measure azimuthal anisotropy by comparing phase velocities from different azimuths for a small region within the array. We choose to only examine anisotropy in the region where the E-W subarray and N-S subarray cross, since this area contains sufficient seismic stations distributed in a 2-D array and crustal thickness variations are minor. In other locations the station geometry is not sufficiently 2-D or, in the case of the Ross Island area, lateral variation in crustal thickness and mantle velocity heterogeneities contaminate anisotropy measurements. The array analysis provides one measure of velocity and azimuth (or the slowness

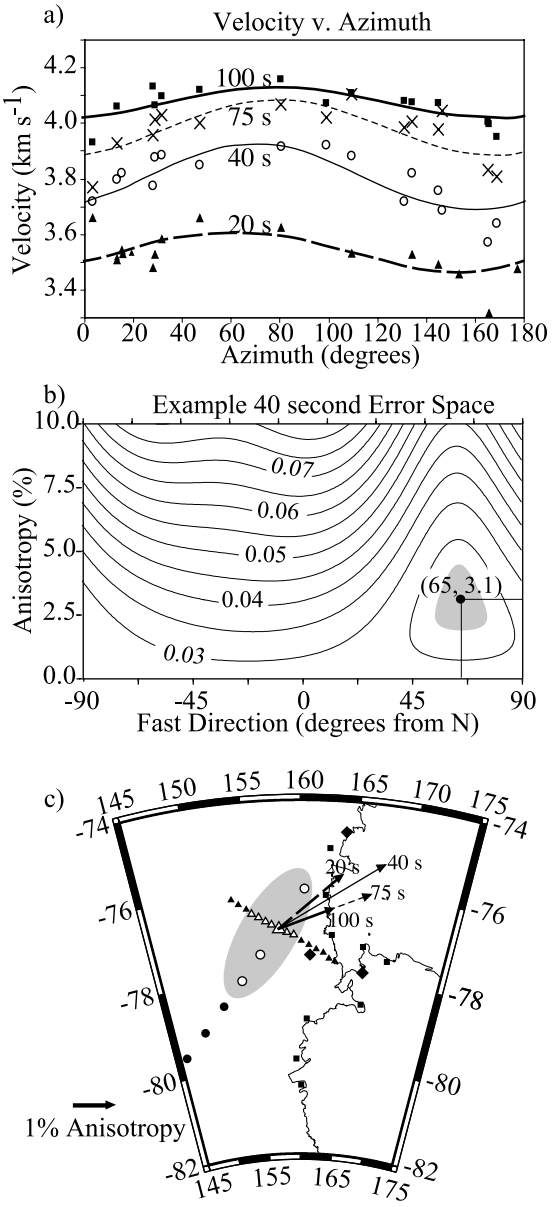

Figure 7. (a) Phase velocity for individual events as a function of back azimuth determined from array analysis using only stations near the intersection of the two linear arrays (Figure 7c, gray shaded area). Phase velocities show a clear sinusoidal pattern with azimuth, which is most pronounced at 40 and 75 s but is still visible for 20 and 100 s. Lines show the best fit azimuthal distribution at each period determined by a grid search. (b) Contour map of the error space at a period of 40 s. The map locates the fast direction and anisotropy magnitude within the 95% confidence interval (gray area). (c) Fast directions for 20, 40, 75, and 100 s on a map of the array.

vector, **p**) for each earthquake and frequency. The inverted value of slowness representing the whole network is better constrained than are the individual interstation phase velocities, so that small variations as a function of azimuth are more easily observed. We perform the array analysis in the small subarray near the intersection (Figure 7, shaded area), extending from N000 to N028 along the NS line and E012 to E024 along the EW line, to prevent large-scale heterogeneity from biasing the result. We only examine earthquakes where at least five high-quality phase velocity curves are obtained to ensure that individual outliers do not adversely change the results. We use a grid search to determine which two parameters (percent anisotropy, γ, and angle of the fast direction, ϕ) best fit a sinusoidal velocity pattern with azimuth. Chi-squared analysis determines the error bounds associated with these two parameters.

[24] Beneath East Antarctica we observe 1.5–3% azimuthal anisotropy with the fast direction between 55 and 85 degrees east of north (Figure 7). This phase velocity anisotropy direction is relatively stable for periods between 20 and 120 s. The 95% confidence interval of the χ-squared test (Figure 7b) indicates that the fast direction and percent anisotropy are accurate to within $\pm 15^\circ$ and $\pm 1\%$ for a period of 40 s. The regional paths are too short for reliable phase velocity calculation at periods longer than 120 s. The maximum azimuthal anisotropy occurs at $\sim$40 s (3.2 $\pm$ 1%) and the minimum occurs at $\sim$120 s (0.7 $\pm$ 0.8%). Beyond 100 s the anisotropy is indistinguishable from zero given a 95% confidence level. The maximum anisotropy direction is consistent with preliminary *SKS* splitting results obtained from the TAMSEIS stations [*Barklage et al.*, 2004].

3.4. Tomographic Inversion for Phase Velocities

[25] We invert the corrected interstation phase velocities for each period with a singular value decomposition inversion of the combined matrix,

$$\begin{bmatrix} \Delta \mathbf{x} \\ \lambda \end{bmatrix} [\mathbf{s}] = \begin{bmatrix} \Delta \mathbf{t} \\ \mathbf{0} \end{bmatrix}, \tag{4}$$

where λ is the first derivative smoothing constraint, and **s** is the slowness vector. Only data with less than 20 degrees difference between the interstation back azimuth and the event-to-station back azimuth are used in the inversion. We use an 808 node 2-D block geometry with 55 km lateral spacing for each period (Figure 3). We invert for slowness with all 808 nodes, but remove the nodes with low (<1% maximum) resolution, as determined by the diagonal elements of the model resolution matrix. We truncate all singular values below 5% of the maximum singular value to reduce the importance of poorly constrained portions of the model space. This results in 357 $\pm$ 46 robust nodes depending on data coverage for each model.

[26] The anisotropic variation is removed by perturbing the apparent interstation phase velocities as a function of azimuth before inversion. The anisotropy was determined for the region where the two arrays intersect, and we have no constraint on the lateral extent of the anisotropic zone. Therefore we calculate two end-member solutions. The first has anisotropy throughout all of East Antarctica, while the second is limited to the regions in which the anisotropy was observed. We calculate 30 different phase velocity maps for periods from 16 to 180 s.

[27] Phase velocity maps for 6 of the 30 calculated periods are shown in Figure 8. The inverted models with anisotropy extending the entire lateral extent of EA do not

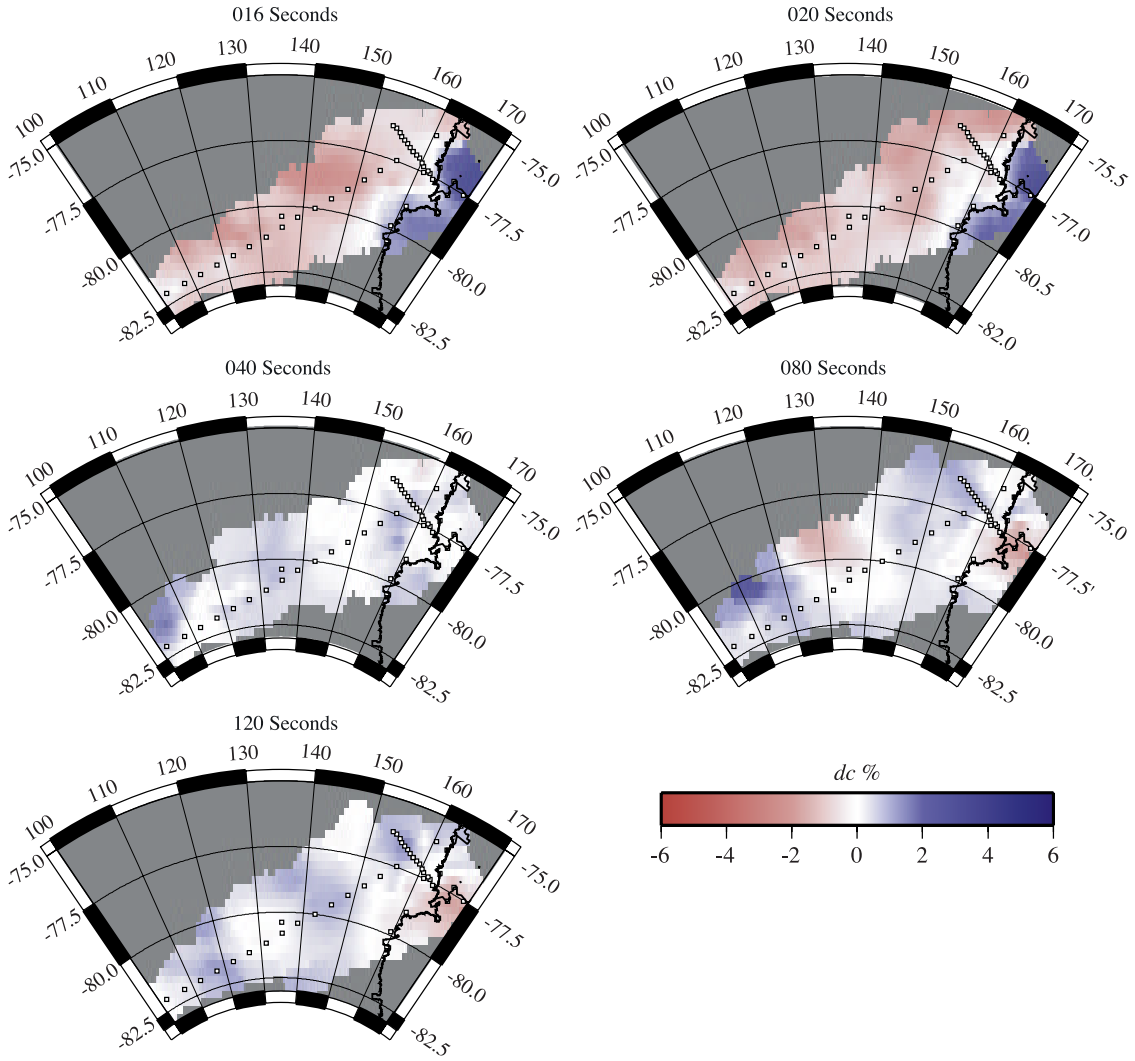

Figure 8. Phase velocity maps corresponding to periods from 16 to 120 s.

significantly reduce the data misfit more than models that limit anisotropy to the region where it is observed. Consequently we only present the models with localized anisotropy. Short-period phase velocity maps (16–25 s) demonstrate a bimodal distribution of velocities having ∼3% low velocity in East Antarctica and ∼4% high in the Ross Sea relative to the regional mean. Intermediate periods (30–60 s) lack a coherent pattern. Instead, this period range gradually changes from the short-period pattern to the longer-period pattern. At longer periods (70–180 s) the Ross Sea is ∼3% slower than East Antarctica with the lowest velocities (−4% relative to the average phase velocity curve) directly beneath Ross Island. Upper mantle velocities from a preliminary body wave tomography study based on TAMSEIS data show a pattern that is similar to the longer-period phase velocity maps [*Watson et al.*, 2004].

[28] Resolution maps plotting a single row of the model resolution matrix (Figures 9a and 9b) show that there is good resolution for the 55 km node spacing we have chosen. While the amplitudes for such small-scale anomalies are sometimes 50% dampened and 200% broadened, the anomalies are clearly located. This is the effect of the smoothing constraint. To test our resolution for larger features, we conducted a series of synthetic tests. The amplitude of a synthetic anomaly similar to the one observed beneath Ross Island with 80 s Rayleigh waves is on average 93% recovered (Figures 9c and 9d) for the resolvable nodes. The amplitude of the dichotomy between East and West Antarctica is on average 88% recovered (Figures 9e and 9f) at 20 s for the resolvable nodes. Figures 10a, 10b, and 10c show how the resolution varies with geographical location by plotting the diagonal elements of the model resolution matrix. As expected, there is generally good resolution near the linear arrays and in the entire region surrounding the array intersection and the coastal array.

4. Discussion

4.1. Crustal Structure

[29] The short-period Rayleigh phase velocity discontinuity between EA and the RS is consistent with a shallow Moho in the RS (∼20 km) and deeper Moho (35–40 km) under the TAMs and EA [*Bannister et al.*, 2003; *Kanao et al.*, 2002]. The shorter-period (16–25 s) Rayleigh waves sample mantle velocities where the crust is thin, such as the Ross Sea, whereas they sample only crustal velocities in

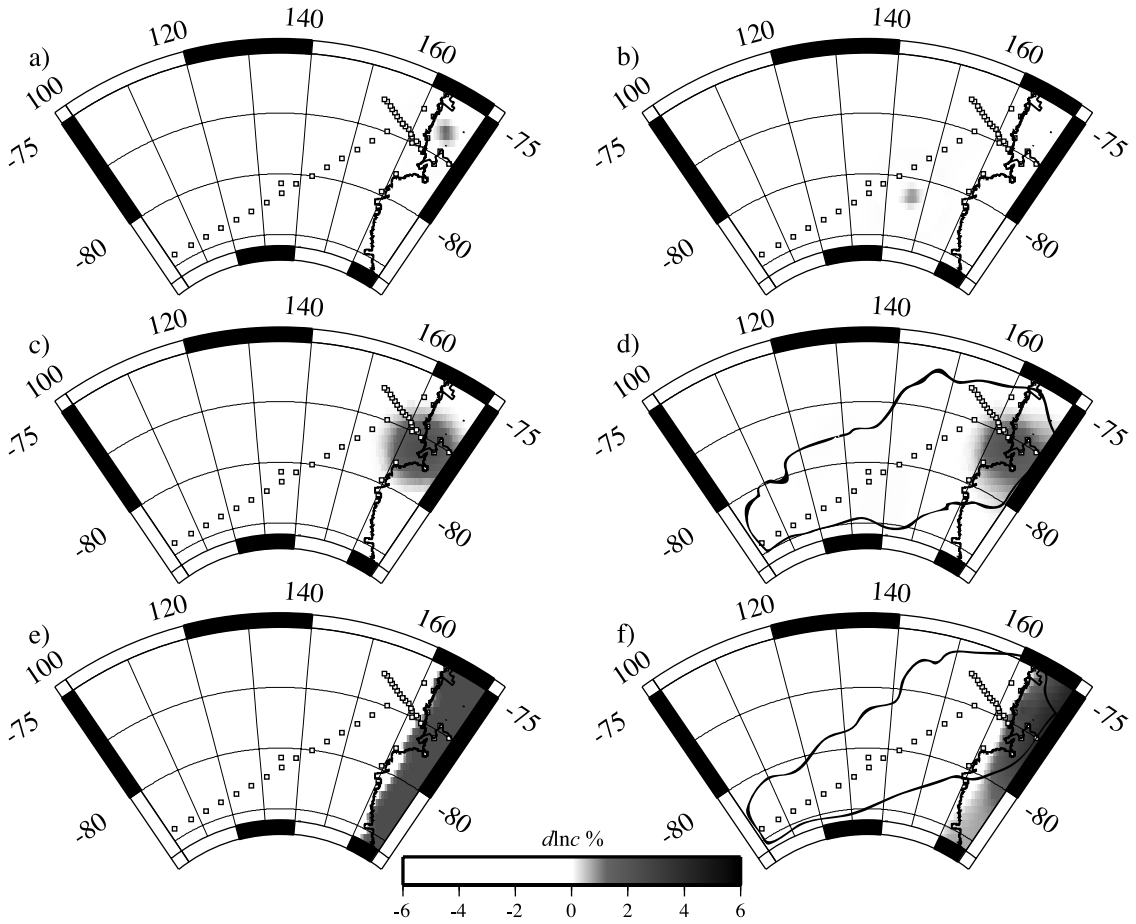

Figure 9. (a and b) Plots of the elements of two rows of the 80 s resolution matrix at their corresponding geographic positions showing that phase velocities are well resolved near the center of the arrays. (c) Synthetic phase velocity anomaly near Ross Island and (d) 80 s recovered velocity anomaly. (e) Synthetic phase velocity anomaly along the coast of the Ross Sea and (f) 20 s recovered velocity anomaly. Figures 9c, 9d, 9e, and 9f show that the observed phase velocity anomalies are well recovered. The outlined regions correspond to the nontruncated nodes displayed in Figure 8.

regions of thicker crust. This transition between fast mantle and slow crust occurs between 25 and 100 km inland from the coast and continues for at least 650 km N-S along the TAMs. Beyond the TAMs in East Antarctica we find little evidence of other velocity anomalies at short periods. The homogeneity of seismic velocity anomalies indicates that the crustal structure is relatively uniform over more than 1000 km distance. This result agrees with the lower resolution results of *Morrelli and Danesi* [2004] and *Ritzwoller et al.* [2001] that showed constant ~35 km thick crust in this region. These general conclusions are also confirmed by receiver function studies of the TAMSEIS data [*Lawrence et al.*, 2004].

4.2. Mantle Velocity Structure

[30] The East Antarctic mantle velocities are 2.5–5% fast relative to PREM from ~80 to 220 km depth (Figure 6b). The seismic velocities in the Ross Sea are ~2.5% slower than PREM between 80 and 180 km depth. The long-period phase velocity maps show that this lateral transition is fairly abrupt and occurs between 50 and 150 km inland from the coast beneath the crest of the TAM. This structure suggests that warmer and buoyant WARS upper mantle extends 50–150 km beneath the TAM and may provide some of the buoyancy necessary for mountain building. The crustal and upper mantle transitions are more precisely imaged in a joint inversion of Rayleigh wave phase velocities and receiver functions and the implications for TAM mountain building are discussed by J. F. Lawrence et al. (Comprehensive seismic and geophysical study of the Transantarctic Mountains, East Antarctica, and the West Antarctic Rift System, submitted to *Geochemistry, Geophysics, Geosystems*, 2006).

[31] The mantle velocities of the RS show a pronounced low-velocity zone extending from ~80 to 220 km depth (Figure 6b), with the lowest velocities of ~4.3 km/s found at depths of 110 to 180 km. The pronounced low-velocity zone suggests that the WARS lithosphere is only about 80–100 km thick. The extensional process that led to crustal thinning of the Ross Sea region [*Fitzgerald et al.*, 1986; *Cooper et al.*, 1987; *DiVenere et al.*, 1994; *Luyendyk et al.*, 1996] and magmatism [*Behrendt*, 1999; *Behrendt et al.*, 1991a, 1991b] may have also modified the lithosphere [*Busetti et al.*, 1999].

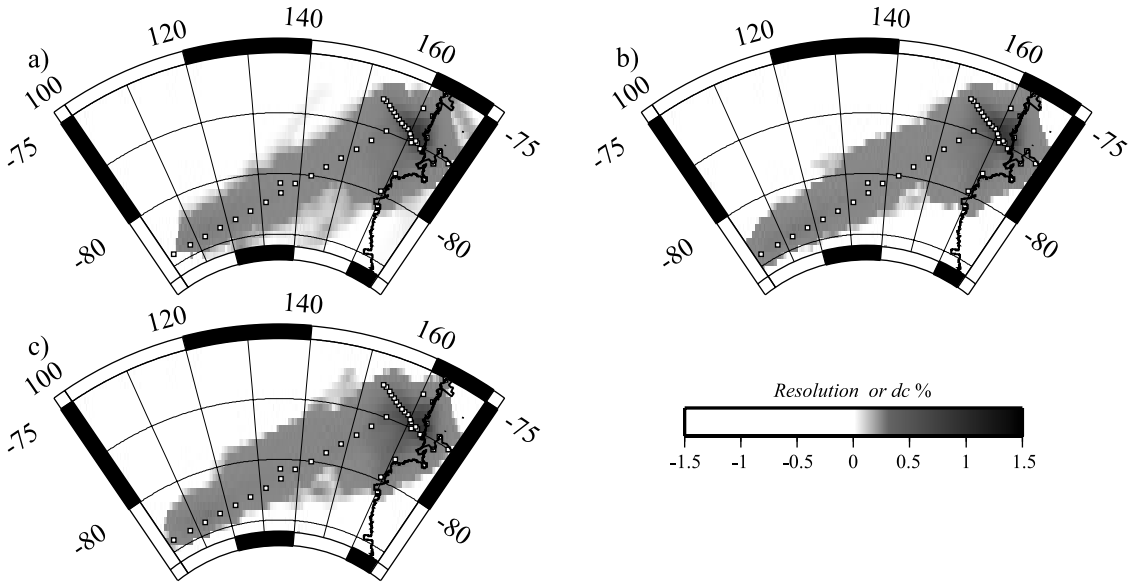

Figure 10. Diagonal elements of the resolution matrix plotted at their corresponding geographic positions for periods of 20 (a), 80 (b), and 120 (c) s. Results show that anomalies near the coastal array, the intersection of the two lines, and along the long station line are well resolved.

[32] The minuscule differences between the 1-D RS velocity model presented here and that of *Ritzwoller et al.* [2001] sampled at the Byrd Subglacial Basin likely arise because of differences in model parameterization, sample locations, and limitations in resolution (Figure 11b). Both studies image shallow low velocities between 80 and 160 km, with more PREM-like structure at greater depths. The similarity between these models indicates that the WARS structure is robust and relatively constant along the TAMs front from Ross Island to the Byrd Subglacial Basin. The large-scale similarity in structure can easily be seen from the vertical cross sections of *Morrelli and Danesi* [2004].

[33] The models of *Bannister et al.* [2000] also demonstrated a rapid change from PREM-like structure beneath the TAMs to structure having low velocity in the asthenosphere in the Ross Sea region. While comparisons between results of this study and those of *Bannister et al.* [2000] are limited by the small amount of data presented by *Bannister et al.* [2000], the velocity perturbations found in each study are remarkably similar. Both studies observed large (2–5%) low-velocity perturbations relative to PREM between ~50 and 200 km depth with the greatest perturbations occurring between ~80 and 160 km depth.

[34] The Ross Sea seismic structure is similar to typical, slow-rifting continental rift structures such as the Rio Grande Rift [*West et al.*, 2004]. While slower than typical Phanerozoic structures, which are similar to PREM (Figure 6b), there is little evidence of very low velocities indicative of plume/melt interaction observed in spreading systems like the East African Rift [*Weeraratne et al.*, 2003] and the Lau Basin [*Xu and Wiens*, 1997]. While this study cannot deny the possibility of larger-amplitude low velocities farther into the Ross Sea, long-wavelength surface wave studies [e.g., *Morrelli and Danesi*, 2004] suggest that the velocities are just as low (or lower), close to the TAMs. Additionally, the Terror Rift (the only rift in the Ross Sea) is adjacent to the TAMs, which suggests that the imaged region should contain the most focused, large-amplitude, low-velocity anomalies within the Ross Sea. Tectonic regions with fast spreading and high degrees of melt often have much lower velocities at shallow depths (<100 km) as seen in the Lau Basin [*Xu and Wiens*, 1997]. The East African rift system [*Weeraratne et al.*, 2003] shows a low-velocity zone at a similar depth, but with velocities that are up to 5% slower. The Rio Grande Rift shows very similar velocities but with the slowest velocities at a somewhat shallower depth [*West et al.*, 2004]. Given recent laboratory and analytical results linking melt and seismic properties [*Hammond and Humphreys*, 2000; *Takei*, 2002; *Faul et al.*, 2004], it seems unlikely that the rather modest slow velocity anomalies observed in the Ross Sea are indicative of widespread partial melt in the asthenosphere. Rather, they probably indicate temperatures near the solidus, resulting in high attenuation and somewhat lower velocities due to subsolidus grain-boundary weakening mechanisms [*Jackson et al.*, 2002]. These more modest low velocities suggest, but cannot prove, that WARS volcanism [e.g., *LeMasurier*, 1989] resulted from passive lithospheric stretching rather than an active plume/melt driven process [*Behrendt et al.*, 1992].

[35] The East Antarctic 1-D model has much higher seismic velocities at depths commonly associated with a low-velocity asthenosphere. Seismic velocities remain nearly constant from the Moho to 250 km depth, with only a very slight decrease at about 150 km depth (Figure 11a). The high velocities are comparable to those found beneath other cratons [*Weeraratne et al.*, 2003; *Freybourger et al.*, 2001], and are faster than the reference model AK135, which represents an average continental structure [*Kennett et al.*, 1995]. The elevated seismic velocities suggest that EA has developed a cold, geochemically depleted continental keel commonly associated with ancient cratons [*Jordan*, 1979; *Forte and Perry*, 2000; *Deschamps et al.*, 2002; *Godey et al.*, 2004]. The continental keel reinforces the

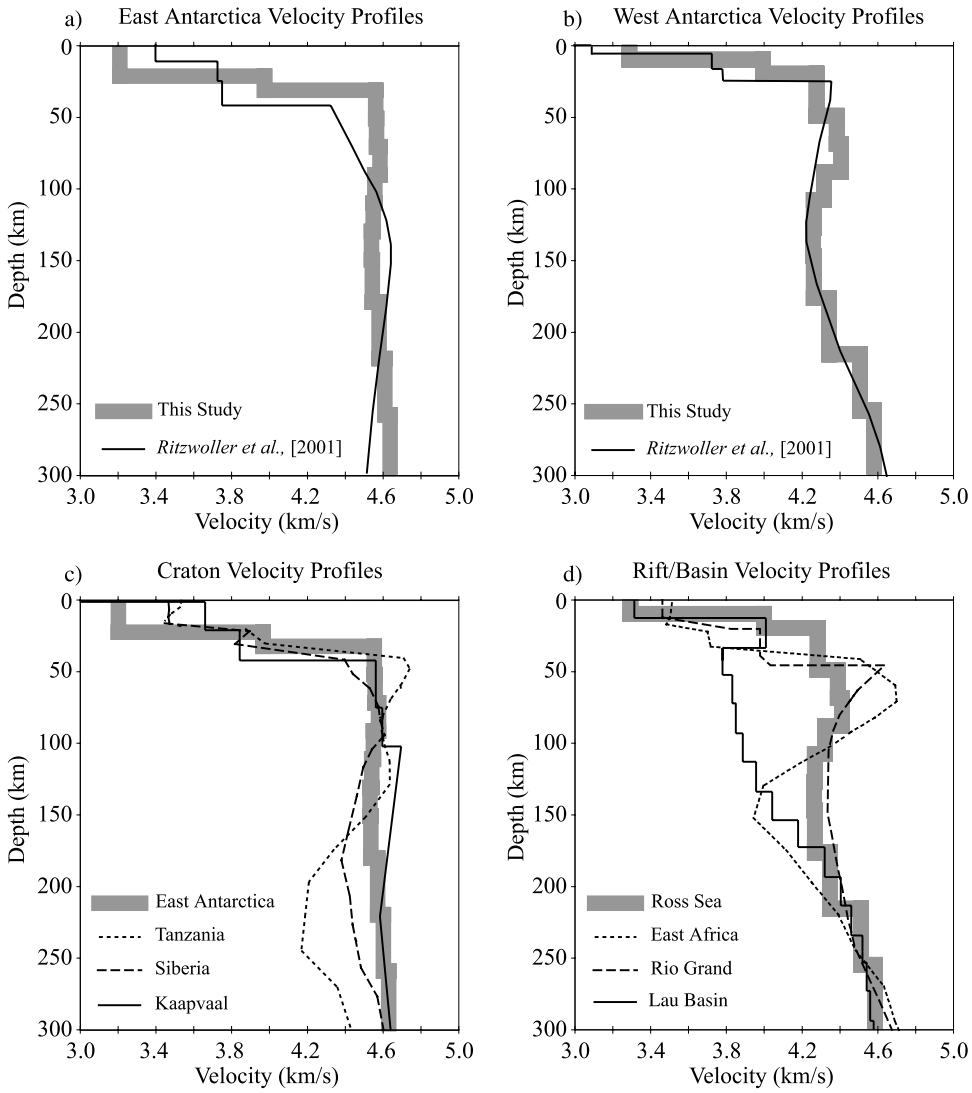

Figure 11. Comparison of the one-dimensional velocity structures from this study (thick gray curves) with those of *Ritzwoller et al.* [2004] (dashed curves) for (a) EA and (b) WARS. (c) EA seismic structure. The EA seismic structure is similar to other cratonic seismic structures, such as Siberia [*Weeraratne et al.*, 2003] and Kaapvaal [*Freybourger et al.*, 2001], but not others, such as Tanzania [*Weeraratne et al.*, 2003]. (d) WARS structure. The WARS structure is similar to the structures of other continental rift systems, such as the Rio Grande [*West et al.*, 2004] and East Africa [*Weeraratne et al.*, 2003], and dissimilar to faster spreading regions, such as the Lau Back Arch Basin [*Xu and Wiens*, 1997].

generally accepted notion that this part of East Antarctica is ancient and not made up of recent orogenic terrains.

[36] The inverted 1-D seismic velocity model calculated for EA agrees with that of *Ritzwoller et al.* [2001] only in that both models possess high seismic velocities bellow ~100 km (Figure 11a). The EA profile of *Ritzwoller et al.* [2001] taken from 80°S and 90°E (west of N132 in the Gamburtsev Subglacial Mountains) overestimates crustal thickness and underestimates shallow mantle velocity compared with our 1-D results. The small differences between these models may be due to unique Gamburtsev Subglacial Mountain (GSM) structure, or simply differences in model parameterization. Because of limitations of resolution in both studies we limit our interpretation.

[37] The thick keel beneath East Antarctica and low velocities in the asthenospheric depth range beneath the Ross Sea suggest a dichotomy in plate behavior. The results presented here agree with attenuation results [*Lawrence et al.*, 2004, 2006], which show that the East Antarctic upper mantle is likely ~300 K colder than that of the RS from 80 to 220 km. The cold, thick lithosphere beneath East Antarctica is consistent with flexural models that require a thick elastic lithosphere (T_e = 85–100 km) and strong flexural rigidity [e.g., *Stern and ten Brink*, 1989; *ten Brink et al.*, 1997]. The warm, thick asthenosphere beneath the Ross Sea likely indicates a weaker plate [*Lawrence et al.*, 2004, 2005], which is also consistent with flexural models [e.g., *ten Brink et al.*, 1997].

4.3. Anomalies Within East Antarctica

[38] Figure 8 shows smaller-scale but still significant phase velocity heterogeneity in East Antarctica, where little

is known about the geological or seismic structure of the lithosphere. The lack of significant velocity anomalies at shorter periods (16–20 s, Figures 8a and 8b) indicates that any changes in crustal thickness must be minor, consistent with results from teleseismic receiver functions [*Lawrence et al.*, 2004]. The EA phase velocities vary more at longer periods (80–120 s), suggesting lateral heterogeneity this area (Figures 8d and 8e). Detailed analyses of individual phase velocity measurements, and tests involving restriction of the data to surface waves with back azimuths nearly along the N-S subarray suggests that these anomalies within East Antarctica are well resolved.

[39] The mantle anomalies within East Antarctica are best resolved at about 80 s, since these periods have more data with shorter path lengths than the longer periods. The 80 s phase velocities are slowest at the western (continentward) edge of the Wilkes Subglacial Basin near stations N60-84, and fastest in the Vostok Subglacial Highlands from N092-N128 and the part of the Wilkes Subglacial Basin just to the west of the TAM (stations N020 to N044).

[40] The lateral variations in phase velocity within EA appear reasonable when compared with velocity anomalies observed in other cratonic regions such as South Africa [*Fouch et al.*, 2004], Australia [*Simons et al.*, 2002], and North America [*van der Lee and Nolet*, 1997]. In each study, small-scale anomalies with amplitudes 1–2% were found within and surrounding cratonic units. Seismic low-velocity and low-density anomalies of 1–2% and 2–3% can result from extensive metasomatism of continental heels [*Jordan*, 1975, 1979]. The low-velocity anomalies observed near N084 and TIMW may be due to iron enrichment caused by reworking of the lithosphere. Indeed, it is possible that extensive reworking may have accompanied volcanism in the Adventure Subglacial Trench (Figure 1), north of the large low-velocity anomaly shown in observed in the 80 s phase velocity map [*Studinger et al.*, 2003]. Such reworking would likely be accompanied by a return to a warmer geotherm.

[41] It is tempting to infer from studies such as the Kaapvaal study that the seismic velocity anomalies delineate boundaries between cores of cratons. It is generally assumed that East Antarctica represents a Proterozoic to Archean cratonic assemblage that has existed intact since Precambrian times, but several studies suggest some Phanerozoic tectonic activity must be considered [*Boger et al.*, 2001; *Fitzsimons*, 2003; *Studinger et al.*, 2003]. Detailed seismological studies of other cratonic regions where good geologic data are available suggest that Phanerozoic mobile belts are readily distinguishable from Precambrian cratons because of their lower upper mantle seismic velocities and lack of a deep, high-velocity cratonic root [*Jordan*, 1979; *Weeraratne et al.*, 2003; *Fouch et al.*, 2004]. Thus one possibility is that the reduced mantle velocity region at the western edge of the Wilkes Subglacial Basin represents a younger suture between two Precambrian cratonic blocks.

[42] However, without a better geologic framework for EA it is difficult to use seismic anomalies to infer terrain boundaries. Some studies show that velocity anomalies within a Precambrian shield region may show little relationship to surface tectonics, suggesting anomalies within the shield may result from the pattern of small-scale convection within the asthenosphere beneath the continental craton [*Rondenay et al.*, 2001; *Shapiro and Ritzwoller*, 2004]. Consequently, resolution of this issue must await better aerogeophysical and geological constraints and improved seismic models for East Antarctic mantle structure.

4.4. Anisotropy and Mantle Fabric of East Antarctica

[43] The anisotropy within East Antarctica just west of the TAM near the junction of the seismic lines has a NE-SW fast direction and is most pronounced at periods of 40–75 s but is detectable between 20 and 120 s (Figure 7). The large range of anisotropic periods is sensitive to a wide range of depths from 30 to ~160 km. Consequently, the anisotropy is not likely localized within a single thin layer, but rather distributed over a broad range of depths within the uppermost mantle. This demonstrates that the anisotropy must result from lattice-preferred orientation [*Zhang and Karato*, 1995] within the relatively cold continental lithosphere. While the shorter periods have sensitivity to crustal anisotropy, anisotropy measurements at periods longer than 40 s (or 60 km) are clearly due to anisotropy in the mantle. The largest anisotropy is measured between 40 and 75 s, suggesting particularly focused strain between 60 and 100 km. Low-amplitude anisotropy (<1 ± 1%) may extend to 160 km as evidenced by anisotropy at 120 s.

[44] Because East Antarctica lacks an asthenospheric low-velocity zone (between 30 and 200 km depth) it is difficult to attribute the observed anisotropy to present-day mantle shear and flow at the base of the current lithosphere within a low-viscosity zone. A thick (>220 km) rigid lithosphere would resist deformation and would not be prone to basal shear within this depth range. Therefore the observed anisotropy is likely due to a relict fabric from past deformational episodes such as the Ross Orogeny. Recent faults found in outcrops throughout the TAMs have been shown to reactivate along NE-SW Paleozoic fabric formed during the Ross Orogeny (~500 Ma) [e.g., *Jones*, 1997]. This demonstrates that, at least for shallow depths, the relic fabric may have been preserved. The 60–100 km range of elevated anisotropy is consistent with the bottom of a typical lithosphere, where anisotropy may have formed as a result of basal shear [e.g., *Bokelmann and Silver*, 2002]. Since the formation of the fabric, the lithosphere likely cooled and thickened to its present rigid state, which aided in the preservation of the ancient anisotropic fabric to the present day.

5. Summary

[45] This phase velocity analysis provides new insight into the lithospheric structure for parts of the West Antarctic rift system (WARS), Transantarctic Mountains (TAMs), and the East Antarctica craton (EA). Short-period phase velocities indicate that the crust abruptly transitions at the coast from thin (~20 km) beneath the Ross Sea to thick (~35 km) beneath East Antarctica. Deeper (~80–220 km) seismic velocities increase westward from the RS region of the WARS through the TAMs and into EA. The transition between fast and slow occurs 100 ± 50 km inland from the coast, beneath the TAMs rather than at the coast. Within the vicinity of the Wilkes Subglacial Basin (EA), we observed 2 ± 1% anisotropy with a NE-SW fast direction for periods between 20 and 120 s (sensitive to depths from

30–160 km). Within EA, low-amplitude phase velocity anomalies may indicate lateral variation in lithospheric structure. However, without a geophysical context, it is difficult to derive the nature of these anomalies.

[46] **Acknowledgments.** We thank Mitchell Barklage, Bruce Beaudoin, Maggie Benoit, James Conder, Audrey Huerta, Bruce Long, Bob Osburn, Tim Parker, Rigobert Tibi, Tim Watson, and many other individuals for assistance in preparing, deploying, and retrieving TAMSEIS stations and data. Portable seismic instruments for this project were obtained from the PASSCAL program of the Incorporated Research Institutions in Seismology (IRIS), and data-handling assistance was provided by the IRIS Data Management System. We also thank the two reviewers for their thorough and helpful reviews. This research was conducted with support from NSF grants OPP9909603 and OPP9909648.

References

Bannister, S., R. K. Sneider, and M. L. Passier (2000), Shear wave velocities under the Transantarctic Mountains and Terror Rift from surface wave inversion, *Geophys. Res. Lett.*, *27*, 281–284.

Bannister, S., J. Yu, B. Leitner, and B. L. N. Kennett (2003), Variations in crustal structure across the transition from West to East Antarctica, Southern Victoria Land, *Geophys. J. Int.*, *155*, 870–880.

Barklage, M., S. Pozgay, J. Lawrence, P. J. Shore, D. A. Wiens, A. Nyblade, S. Anandakrishnan, and D. Voigt (2004), Upper mantle seismic anisotropy of the Ross Sea, Trans-Antarctic Mountains, and East Antarctica from SKS splitting analysis, *Eos Trans. AGU*, *85*(47), Fall Meet. Suppl., Abstract T11A-1228.

Behrendt, J. C. (1999), Crustal and lithospheric structure of the West Antarctic rift system from geophysical investigations—A review, *Global Planet. Change*, *23*, 25–44.

Behrendt, J. C., H. J. Duerbaum, D. Damaske, R. Saltus, W. Bosum, and A. K. Cooper (1991a), Extensive volcanism and related tectonism beneath the Ross Sea continental shelf, Antarctica: Interpretation of an aeromagnetic survey, in *Geological Evolution of Antarctica*, edited by M. R. A. Thompson, J. A. Crame, and J. W. Thomson, pp. 299–304, Cambridge Univ. Press, New York.

Behrendt, J. C., W. E. LeMasurier, A. K. Cooper, F. Tessensohn, A. Trehu, and D. Damaske (1991b), Geophysical studies of the West Antarctic rift system, *Tectonics*, *10*, 1257–1273.

Behrendt, J. C., W. E. LeMasurier, and A. K. Cooper (1992), The West Antarctic rift system—A propagating rift "captured" by a mantle plume, in *Recent Progress in Antarctic Earth Science*, edited by K. Kaminuma and Y. Yoshida, pp. 315–322, Terra Sci., Tokyo.

Bentley, C. R. (1991), Configuration and structure of the subglacial crust, in *The Geology of Antarctica*, edited by R. J. Tingey, pp. 335–364, Clarendon, Oxford, U. K.

Boger, S. D., C. J. L. Wilson, and C. M. Fanning (2001), Early Paleozoic tectonism within the East Antarctic craton: The final suture between east and west Gondwana?, *Geology*, *29*, 463–466.

Bokelmann, G. H. R., and P. G. Silver (2002), Shear stress at the base of shield lithosphere, *Geophys. Res. Lett.*, *29*(23), 2091, doi:10.1029/2002GL015925.

Brancolini, G., et al. (1995), Seismic stratigraphic atlas of the Ross Sea, Antarctica, in *Geology and Seismic Stratigraphy of the Antarctic Margin*, *Antarctic Res. Ser.*, vol. 68, edited by A. K. Cooper, P. F. Barker, and G. Brancolini, pp. 271–286, AGU, Washington, D. C.

Busetti, M., G. Spadini, F. M. Van der Wateren, S. Cloetingh, and C. Zanolla (1999), Kinematic modeling of the West Antarctic rift system, Ross Sea, Antarctica, in *Global and Planetary Change*, edited by F. M. van der Wateren and S. A. P. L. Cloetingh, pp. 79–103, Elsevier, New York.

Cogley, J. G. (1984), Deglacial hypsometry of Antarctica, *Earth Planet. Sci. Lett.*, *67*, 151–177.

Cooper, A. K., F. J. Davey, and J. C. Behrendt (1987), Seismic stratigraphy and structure of the Victoria Land Basin, western Ross Sea, Antarctica, in *The Antarctic Continental Margin: Geology and Geophysics of the Western Ross Sea*, edited by A. K. Cooper and F. J. Davey, pp. 27–76, Circum-Pac. Counc. for Energ. and Nat. Res., Houston, Tex.

Cooper, A. K., H. Trey, G. Cochrane, F. Egloff, M. Busetti, and Acrup Working Group (1997), Crustal structure of the southern Central Trough, western Ross Sea, in *The Antarctic Region: Geological Evolution and Processes: Proceedings of the 7th International Symposium on Antarctic Earth Sciences, Siena 1995*, edited by C. A. Ricci, pp. 637–642, Terra Antarct., Siena, Italy.

Dalziel, I. W. D. (1992), Antarctica: A tale of two supercontinents, *Annu. Rev. Earth Planet. Sci.*, *20*, 501–526.

Danesi, S., and A. Morelli (2001), Structure of the upper mantle under the Antarctic Plate from surface wave tomography, *Geophys. Res. Lett.*, *28*, 4395–4398.

Davey, F. J. (1981), Geophysical studies of the Ross Sea region, *J. R. Soc. N. Z.*, *11*, 465–479.

Deschamps, F., J. Trampert, and R. Snieder (2002), Anomalies of temperature and iron in the uppermost mantle inferred from gravity data and tomographic models, *Phys. Earth Planet Inter.*, *129*, 245–264.

DiVenere, V. J., D. V. Kent, and I. W. D. Dalziel (1994), Mid-Cretaceous paleomagnetic results from Marie Byrd Land, West Antarctica: A test of post-100 Ma relative motion between East and West Antarctica, *J. Geophys. Res.*, *99*, 15,115–15,139.

Dziewonski, A. M., and D. L. Anderson (1981), Preliminary reference Earth model, *Phys. Earth Planet. Inter.*, *25*, 297–356.

Dziewonski, A. M., S. Bloch, and M. Landisman (1969), A technique for the analysis of transient seismic signals, *Bull. Seismol. Soc. Am.*, *59*, 427–444.

Faul, U. H., J. D. Fitz Gerald, and I. Jackson (2004), Shear wave attenuation and dispersion in melt-bearing olivine polycrystals: 2. Microstructural interpretation and seismological implications, *J. Geophys. Res.*, *109*, B06202, doi:10.1029/2003JB002407.

Fitzgerald, P. G., M. Sandiford, P. J. Barret, and J. W. Gleadow (1986), Asymmetric extension associated with uplift and subsidence in the Transantarctic Mountains and Ross Embayment, *Earth Planet. Sci. Lett.*, *81*, 67–78.

Fitzsimons, I. C. W. (2003), Proterozoic basement provinces of southern and southwestern Australia, and their correlation with Antarctica, in *Proterozoic East Gondwana: Supercontinent Assembly and Break-up*, edited by M. Yoshida, B. F. Windley, and S. Dasgupta, *Geol. Soc. Spec. Publ.*, *206*, 184–208.

Forte, A. M., and A. C. Perry (2000), Seismic-geodynamic evidence for a chemically depleted continental tectosphere, *Science*, *290*, 1940–1944.

Fouch, M. J., D. E. James, J. C. VanDecar, and S. van der Lee (2004), Mantle seismic structure beneath the Kaapvaal and Zimbabwe cratons, *S. Afr. J. Geol.*, *107*, 33–44.

Freybourger, M., J. B. Gaherty, T. H. Jordan, and the Kaapvaal Seismic Group (2001), Structure of the Kaapvaal craton from surface waves, *Geophys. Res. Lett.*, *28*, 2489–2492.

Godey, S., F. Deschamps, J. Trampert, and R. Sneider (2004), Thermal and compositional anomalies beneath the North American continent, *J. Geophys. Res.*, *109*, B01308, doi:10.1029/2002JB002263.

Groushinsky, N. P., and N. B. Sazhina (1982), Some features of Antarctic crustal sructure, in *Antarctic Geoscience—Symposium on Antarctic Geology and Geophysics, Madison, Wisconsin*, edited by C. Craddock, pp. 907–911, Univ. of Wis. Press, Madison.

Hammond, W. C., and E. D. Humphreys (2000), Upper mantle seismic wave velocity: Effects of realistic partial melt geometries, *J. Geophys. Res.*, *105*, 10,975–10,986.

Herrin, E., and T. Goforth (1977), Phase-matched filters: Application to the study of Rayleigh waves, *Bull. Seismol. Soc. Am.*, *67*, 1259–1275.

Jackson, I., J. D. Fitz Gerald, U. H. Faul, and B. H. Tan (2002), Grain-size-sensitive seismic wave attenuation in polycrystalline olivine, *J. Geophys. Res.*, *107*(B12), 2360, doi:10.1029/2001JB001225.

Jones, S. (1997), Late quaternary faulting and neotectonics, South Victoria Land, Antarctica, *J. Geol. Soc.*, *154*, 645–652.

Jordan, T. H. (1975), The continental tectosphere, *Rev. Geophys.*, *13*, 1–12.

Jordan, T. H. (1979), Mineralogies, densities and seismic velocities of garnet, Lherzolites and their geophysical implications, in *The Mantle Sample: Inclusions in Kimberlites and Other Volcanics—Proceedings of the Second International Kimberlite Conference*, edited by F. R. Boyd and H. O. A. Meyer, pp. 1–14, AGU, Washington, D. C.

Kanao, M., A. Kubo, T. Shibutani, H. Negishi, and Y. Tono (2002), Crustal structure around the Antarctic margin by teleseismic receiver function analyses, in *Antarctica at the Close of a Millennium*, edited by J. A. Gamble, D. N. B. Skinner, and S. Henrys, *R. Soc. N. Z. Bull.*, *35*, 485–491.

Kennett, B. L. N., E. R. Engdahl, and R. Buland (1995), Constraints on seismic velocities in the Earth from travel times, *Geophys. J. Int.*, *122*, 108–124.

Koper, K. D., M. E. Wysession, and D. A. Wiens (1999), Multimodal function optimization with a niching genetic algorithm: A seismological example, *Bull. Seismol. Soc. Am.*, *89*, 978–988.

Kyle, P. R., J. A. Moore, and M. F. Thirlwall (1992), Petrologic evolution of anorthoclase phonolite lavas at Mount Erebus, Ross Island, Antarctica, *J. Petrol.*, *33*, 849–875.

Lawrence, J. F., and D. A. Wiens (2004), Combine receiver-function and surface wave phase-velocity inversion using a niching genetic algorithm: Application to Patagonia, *Bull. Seismol. Soc Am.*, *94*, 977–987.

Lawrence, J. F., D. A. Wiens, A. A. Nyblade, S. Anandakrishnan, P. J. Shore, and D. Voigt (2004), Comprehensive seismic and geophysical

study of the Transantarctic Mountains, *Eos Trans. AGU*, *85*(47), Fall Meet. Suppl., Abstract T14A-08.

Lawrence, J. F., D. A. Wiens, A. A. Nyblade, S. Anandakrishnan, P. J. Shore, and D. Voigt (2006), Upper mantle thermal variations beneath the Transantarctic Mountains inferred from teleseismic S-wave attenuation, *Geophys. Res. Lett.*, *33*, L03303, doi:10.1029/2005GL024516.

LeMasurier, W. E. (1989), Late Cenozoic volcanism on the Antarctic Plate—An overview, in *Volcanoes of the Antarctic Plate and Southern Oceans*, *Antarct. Res. Ser.*, vol. 48, edited by W. E. LeMasurier and J. W. Thompson, pp. 1–11, AGU, Washington, D. C.

Luyendyk, B., S. Cisowski, C. Smith, S. Ricard, and D. Kimbrough (1996), Paleomagnetic study of northern Ford ranges, western Marie Byrd Land, West Antarctica: Motion between East and West Antarctica, *Tectonics*, *15*, 122–141.

Lythe, M. B., D. G. Vaughan, and B. Consortium (2001), BEDMAP: A new ice thickness and subglacial topographic model of Antarctica, *J. Geophys. Res.*, *106*, 11,335–11,351.

Mahfoud, S. W. (1995), Niching methods for genetic algorithms, Ph.D. thesis, Univ. of Ill., Champaign.

Menke, W., and V. Levin (2002), Anomalous seaward dip of the lithosphere-asthenosphere boundary beneath northeastern USA detected using differential-array measurements of Rayleigh waves, *Geophys. J. Int.*, *149*, 414–422.

Morrelli, A., and S. Danesi (2004), Seismological imaging of the Antarctic continental lithosphere: A review, *Global Planet. Change*, *42*, 155–165.

Ritzwoller, M. H., N. M. Shapiro, A. L. Levshin, and G. M. Leahy (2001), Crustal and upper mantle structure beneath Antarctica and surrounding oceans, *J. Geophys. Res.*, *106*, 30,645–30,670.

Rondenay, S., M. G. Bostock, and J. Shragge (2001), Multiparameter two-dimensional inversion of scattered teleseismic body waves: 3. Application to the Cascadia 1993 data set, *J. Geophys. Res.*, *106*, 30,795–30,807.

Roult, G., and D. Rouland (1994), Antarctica II: Upper mantle structure from velocities and anisotropy, *Phys. Earth Planet. Inter.*, *84*, 33–57.

Shapiro, N. M., and M. H. Ritzwoller (2004), Inferring surface heat flux distributions guided by a global seismic model: Particular application to Antarctica, *Earth Planet. Sci. Lett.*, *223*, 213–224.

Simons, F. J., R. D. van der Hilst, J.-P. Monagner, and A. Zielhuis (2002), Multimode Rayleigh wave inversion for heterogeneity and azimuthal anisotropy of the Australian upper mantle, *Geophys. J. Int.*, *151*, 738–754.

Stern, T. A., and U. S. ten Brink (1989), Flexural uplift of the Transantarctic Mountains, *J. Geophys. Res.*, *94*, 10,315–10,330.

Storey, B. C. (1996), Microplates and mantle plumes in Antarctica, *Terra Antarct.*, *3*, 91–102.

Studinger, M., G. D. Karner, R. E. Bell, V. Levin, C. A. Raymond, and A. A. Tikku (2003), Geophysical models for the tectonic framework of the Lake Vostok region, East Antarctica, *Earth Planet. Sci. Lett.*, *216*, 663–677.

Takei, Y. (2002), Effect of pore geometry on V_p/V_s: From equilibrium geometry to crack, *J. Geophys. Res.*, *107*(B2), 2043, doi:10.1029/2001JB000522.

ten Brink, U. S., S. Bannister, B. C. Beaudoin, and T. A. Stern (1993), Geophysical investigations of the tectonic boundary between East and West Antarctica, *Science*, *261*, 45–50.

ten Brink, U. S., R. I. Hackney, S. Bannister, T. A. Stern, and Y. Makovsky (1997), Uplift of the Transantarctic Mountains and the bedrock beneath the East Antarctic ice sheet, *J. Geophys. Res.*, *102*, 27,603–27,621.

Tingley, R. J. (1991), *The Geology of Antarctica*, Oxford Univ. Press, New York.

van der Lee, S., and G. Nolet (1997), Upper mantle *S* velocity structure of North America, *J. Geophys. Res.*, *102*, 22,815–22,838.

Watson, T., A. M. Larson, A. Nyblade, M. Benoit, D. A. Wiens, P. Shore, and D. Voigt (2004), Upper mantle structure beneath the Transantarctic Mountains from body-wave tomography and receiver functions using TAMSEIS data, *Eos Trans. AGU*, *85*(47), Fall Meet. Suppl., Abstract T11A-1226.

Weeraratne, D. S., D. W. Forsyth, K. M. Fischer, and A. A. Nyblade (2003), Evidence for an upper mantle plume beneath the Tanzanian craton from Rayleigh wave tomography, *J. Geophys. Res.*, *108*(B9), 2427, doi:10.1029/2002JB002273.

West, M., J. Ni, W. S. Baldridge, D. Wilson, R. Aster, W. Gao, and S. Grand (2004), Crust and upper mantle shear wave structure of the southwest United States: Implications for rifting and support for high elevation, *J. Geophys. Res.*, *109*, B03309, doi:10.1029/2003JB002575.

Xu, Y., and D. A. Wiens (1997), Upper mantle structure of the southwest Pacific from regional waveform inversion, *J. Geophys. Res.*, *102*, 27,439–27,451.

Zhang, S., and S.-I. Karato (1995), Lattice preferred orientation of olivine aggregates deformed in simple shear, *Nature*, *375*, 774–777.

S. Anandakrishnan, A. A. Nyblade, and D. Voigt, Department of Geosciences, Pennsylvania State University, State College, PA 16802, USA.

J. F. Lawrence, Scripps Institute of Oceanography, University of California, San Diego, La Jolla, CA 92093-0225, USA. (jlawrence@ucsd.edu)

P. J. Shore and D. A. Wiens, Department of Earth and Planetary Sciences, Washington University, St. Louis, MO 63130, USA.